Journal of Materials Chemistry A

Accepted Manuscript

ROYAL SOCIETY OF CHEMISTRY

www.rsc.org/materialsA

Journal of Materials Chemistry A

ARTICLE

Solution-Based Synthesis and Characterization of Earth Abundant $Cu_3(As,Sb)Se_4$ Nanocrystal Alloys: Towards Scalable Room-Temperature Thermoelectric Devices

Received 00th January 20xx,
Accepted 00th January 20xx

DOI: 10.1039/x0xx00000x

www.rsc.org/

Robert B. Balow,[a] Edward P. Tomlinson,[b] Mahdi M. Abu-Omar[a,b], Bryan W. Boudouris,[b] and Rakesh Agrawal[b]

A simple and scalable solution-based synthesis route for impurity free $Cu_3(As,Sb)Se_4$ nanocrystal alloys is reported. Additionally, a heat treatment process that eliminates many scalability limitations imposed by traditional sintering methods has been demonstrated to significantly improve both the grain structure and electronic properties of the $Cu_3(As,Sb)Se_4$ nanocrystal based thin films. The combination of a new synthetic pathway with a robust thin film processing methodology offers the promise of widespread application of these materials to many fields. We demonstrate the potential of this material system in a proof-of-concept energy conversion application. Here, the processed $Cu_3(As,Sb)Se_4$ nanocrystal thin films serve as room temperature thermoelectric materials demonstrating a large thermoelectric performance after heat treatment.

[a] Department of Chemistry, Purdue University, 560 Oval Drive, West Lafayette, IN 47907, United States
[b] School of Chemical Engineering, Purdue University, 480 Stadium Mall Drive, West Lafayette, IN 47907, United States

Electronic Supplementary Information (ESI) available: Optimization of heat treatment conditions and atmospheres and SEM-EDS elemental maps of all nanocrystal compositions. SEM-EDS, XRD, Raman spectra of post heat treated films and Raman spectra of the high temperature copper, arsenic and selenium phase is also provided. See DOI: 10.1039/x0xx00000x

Introduction

In the United States, over half the energy used every day is lost as a consequence of poor energy conversion efficiency.[1] The majority of this waste energy is released as heat from industrial processes, electricity production and transportation. This massive energy reserve could be converted directly to electricity by thermoelectric devices. Unfortunately, the high cost and modest conversion efficiencies of many thermoelectric materials have hindered widespread adoption of this heat reclamation strategy.[2] As a result, significant interest in developing and improving low-cost and scalable thermoelectric technologies has emerged.

The performance of thermoelectric materials is evaluated by the dimensionless figure of merit (zT), which is defined as follows.

$$zT = \sigma S^2 T/\kappa$$

Here, T, S, σ, and κ are the absolute temperature, Seebeck coefficient (or thermopower), electrical conductivity, and thermal conductivity, respectively.[3] In traditional bulk thermoelectric materials, there is competition between electrical conductivity and thermopower, which can make optimizing thermoelectric performance challenging.[4,5] Additionally, the thermal conductivity of bulk materials can increase with increasing electrical conductivity due to thermal energy carried by charge carriers.[4,5] Many strategies to increase the figure of merit of these bulk materials have typically consisted of reducing thermal conductivity through phonon scattering mechanisms traditionally achieved by alloying. As a result, several material systems [e.g. $Bi_{0.5}Sb_{1.5}Te_3$ (alloy of Bi_2Te_3 and Sb_2Te_3) and $(PbTe)_{1-x}(CdTe)_x$] have demonstrated great success using this approach.[6,7]

Along a similar line of reasoning, nanoparticle and nanostructured thermoelectric devices have recently gained significant recognition for their ability to further enhance thermoelectric device performance and, in some instances, exceeded in areas where bulk thermoelectric materials have struggled.[8] Nanoparticle based thermoelectric devices present an additional opportunity to scatter phonons through the large number of grain boundaries, which effectively reduces the thermal conductivity and significantly increases zT values in many systems.[9–13]. Moreover by the same effect, nanoparticle alloys have also shown great success in increasing the figure of merit.[14–16]

Top-down production methods of many high performing thermoelectric nanomaterials have been demonstrated, but these routes require energy-intensive and time-consuming methods (*e.g.*, ball milling)[17] raising concerns regarding potential scalability of the materials for widespread application. Furthermore, scalability of these processes are also limited due to the rare and costly element tellurium, which is often incorporated in many of the highest performing thermoelectric materials.[8,17–20] Conversely, solution based nanocrystal (NC) synthesis provides a low-cost and rapid production route to thermoelectric materials due to the NCs being colloidally suspendible in a variety of solutions to form an "ink", which can be quickly printed or spray-coated to produce thin films of thermoelectric materials. This in turn enables high-throughput manufacturing methods (*e.g.*, roll-to-roll processing) and lower production costs.[21,22] Successful production of industrially-viable thermoelectric materials will likely require coupling scalable synthesis process and materials composed of earth abundant elements.

Recently, Cu_3SbSe_4 has been discussed in the literature as a promising thermoelectric material due to its low-cost and competitive figure of merit. Cu_3SbSe_4 has been produced by both top-down and bottom up methods such as mechanical alloying,[16] fusion of elements,[23] and co-precipitation synthesis.[24] Doping Cu_3SbSe_4 with Ge,[25] Sn[24] and Bi[15] has been reported in the literature as a successful means of increasing the figure of merit for this material. In addition, chalcogen alloying ($Cu_3Sb(S,Se)_4$) was also shown to be effective for enhancing the figure of merit.[26,27] Previously reported bulk nanostructured Cu_3SbSe_4 resulted in the highest figure of merit reported to date for Cu_3SbSe_4.[24] Unfortunately, lack of solution processability and the requirement of hot pressing or spark plasma sintering complicates industrial practicality due to the complex nature of these production procedures.

To address these critical issues, we report the first scalable solution-based NC synthesis of a next-generation series of earth abundant Cu_3AsSe_4 and $Cu_3(As,Sb)Se_4$ alloys over a wide range of As and Sb compositions. Furthermore, we describe a unique and scalable heat treatment that avoids the production limitations imposed by more traditional sintering methods such as hot-pressing and spark plasma sintering. Notably, a high degree of system tunability can be afforded by utilizing these syntheses and processing procedures allowing for exploration of this material system in a variety of applications. As a proof-of-concept, we demonstrate a significant thermoelectric performance from the $Cu_3(As,Sb)Se_4$ NCs following a simple heat treating process.

Experimental

Materials and Methods

Reagents. Copper (I) chloride (99.999%, CuCl) was obtained from Strem. Arsenic trichloride (99.99%, $AsCl_3$), antimony trichloride (99.95%, $SbCl_3$), selenium pellets (99.99%, Se), sulfur (99.99%, S), and ethanethiol (97%, ET) were obtained from Sigma-Aldrich. Oleylamine (80-90%, OLA) was obtained from Acros Organics. Ethanol (200-proof) was obtained from Koptec and toluene (99.5%) was purchased from Macron Chemicals. All reagents were used as received except for OLA, which was degassed by three freeze-pump-thaw cycles prior to being stored in an inert environment.

Preparation of the Selenium Precursor Complex. The selenium precursor (Se-OLA) was prepared using a modified dissolution procedure reported previously.[28] Selenium powder (1.43 g, 18.1 mmol) was added to a round bottom flask with a

magnetic stir bar. Oleylamine (18.1 mL) was added to the flask followed by 1.8 mL of ethanethiol. The flask was connected to an inert atmosphere and vacuum (Schlenk) line, vigorously stirred, and gently evacuated and refilled with argon five times. The flask was stirred for 15 min and was then evacuated with stirring for 1 h to remove any residual ET. The flask was then sealed and the Se-OLA was stored under nitrogen until it was ready to use.

Synthesis of Cu_3AsSe_4 Nanocrystals. To a reaction flask equipped with a condenser and magnetic stir bar, 99.0 mg (1.0 mmol CuCl), 7.0 mL of OLA and 30.1 µL (0.357 mmol) of $AsCl_3$ were added. The flask was sealed and attached to an inert atmosphere line. The flask was evacuated and refilled three times with argon. Under an argon blanket, the temperature of the flask was rapidly increased to 125 °C while the solution was stirred. Once at 125 °C, 2.8 mL of Se-OLA were rapidly injected into the flask. The temperature of the flask was then increased to 200 °C and the reaction proceeded for 30 min. After this time, the heating mantle was removed from the flask and the reaction mixture cooled through free convection to ~40 °C. The reaction mixture was then opened to air and the reaction products were washed according the procedure detailed below.

Synthesis of Cu_3SbSe_4 Nanocrystals. To a reaction flask equipped with a condenser and magnetic stir bar, 99.0 mg (1.0 mmol) CuCl, 7.0 mL of OLA and 81.4 mg (0.357 mmol) of $SbCl_3$ were added. The flask was sealed and attached to an inert atmosphere line. The flask was evacuated and refilled three times with argon. Under an argon blanket, the temperature of the flask was rapidly increased to 250 °C with stirring. The flask was held at 250 °C for 2 min, at which point 2.8 mL of Se-OLA was rapidly injected into the flask. The temperature of the flask was maintained at 250 °C for 30 min. After this time, the heating mantle was removed from the flask and the reaction mixture cooled through free convection to ~40 °C. The reaction mixture was then opened to air and the reaction products were washed according the procedure detailed below.

Synthesis of $Cu_3(As,Sb)Se_4$ Nanocrystals. The mixed composition $Cu_3(As,Sb)Se_4$ NCs were synthesized and washed following the previously-described Cu_3SbSe_4 NC procedure except both arsenic trichloride and antimony trichloride precursors were added to the reaction flask for a combined molar sum of 0.357 mmol. More specifically, the $Cu_3(As_{0.25},Sb_{0.75})Se_4$ NCs were synthesized using 22.5 µL (0.268 mmol) of $AsCl_3$ and 20.3 mg (0.089 mmol) of $SbCl_3$. The $Cu_3(As_{0.5},Sb_{0.5})Se_4$ NCs were synthesized using 15.0 µL (0.179 mmol) of $AsCl_3$ and 40.8 mg (0.179 mmol) of $SbCl_3$. The $Cu_3(As_{0.75},Sb_{0.25})Se_4$ NCs were synthesized using 7.5 µL (0.089 mmol) of $AsCl_3$ and 61.1 mg (0.268 mmol) $SbCl_3$.

Washing Procedure and Selenium Etch. The cooled reaction products were pipetted into a 30 mL centrifuge tube, topped with ethanol, vortexed for 10 s and centrifuged at 14,000 rpm for 1 min. The light yellow supernatant was discarded and the pelleted precipitate was re-suspended with ~5 mL of hexane and vortexed for 10 s. The centrifuge tube was then topped with ethanol, vortexed, and centrifuged at 14,000 rpm for 1 min. To selectively etch any unreacted selenium remaining from the reaction, 2.0 mL of OLA and 0.2 mL of ET were added to the centrifuge tube, vortexed for 10 s and centrifuged at 14,000 rpm for 1 min. The dark supernatant was discarded, and, again, 2.0 mL of OLA and 0.2 mL of ET were added to the centrifuge tube, vortexed and centrifuged at 14,000 rpm for 1 min. The transparent yellow supernatant was discarded and the particles were re-suspended and precipitated using hexane and ethanol as previously described two additional times. The NCs were re-suspended with 4 mL toluene and stored.

Thin Film Fabrication and Heat Treatment. Films for thermoelectric measurements were fabricated by drop-casting the desired NCs suspended in toluene onto glass substrates. The samples were slowly dried in air for about 8 h. The $Cu_3(As,Sb)Se_4$ thin film samples were then placed on a hotplate with 6 selenium pellets (c.a. 340 mg) in ceramic trays. A glass bell jar was placed over the samples and selenium-holding trays on the hotplate and the system was evacuated and refilled with nitrogen three times to purge the bell jar of oxygen. The pressure was adjusted to 100 Torr and the hotplate temperature was increased to 340 °C. Once at temperature, the samples were sintered for 30 min in the selenium vapor environment. After this time, the samples were cooled to room temperature via natural convection. Gold contacts (~100 nm in thickness) were deposited on the corners of the film by thermal evaporation under a high vacuum environment.

Electrical Conductivity Measurements. The sheet resistance values of the NC thin films were determined by the four point van der Pauw method after being heated to 313 K. Eight measurements were performed allowing for every possible combination of electrodes. A Keithley 2450 sourcemeter was used to sweep current between two contacts while simultaneously recording voltage on the opposing two contacts. A representative measurement showing the raw data is seen in Figure S1. Electrical conductivity values were calculated after determining film thickness by profilometry using an Alpha-Step D100 surface profilometer.

Thermopower Measurements. The thin film thermopower values were obtained by inducing a temperature gradient using a homemade stage composed of two heating blocks. Temperature data were gathered directly on the thin film using two T-type thermocouples. The electric potentials induced as the result of 7 temperature gradients (*i.e.*, from -15 to 15 K) were collected with a Keithley 2450 sourcemeter. The average temperature for each of the temperature gradients used was 313 K. Five data points were obtained for each temperature gradient for a total of 35 data points per film.

Characterization

Grazing incidence X-ray diffraction (GIXRD) data were collected using a Rigaku SmartLab diffractometer with an incidence angle of 0.5° in a parallel beam geometry with a Cu Kα X-ray source. Raman spectra were acquired using a Horiba/Jobin-Yvon LabRAM HR800 confocal microscope with a 633-nm He:Ne laser through a 100x objective lens. Scanning electron microscopy (SEM) images and scanning electron microscopy energy dispersive X-ray spectroscopy data (SEM-EDS) were obtained using a FEI Quanta 3D FEG Dual-beam field emission scanning electron microscope. To reduce charging-related distortion of the cross-sectional SEM images, ~2 nm of platinum were sputtered-coated on the films. The SEM images were obtained with an electron beam energy of 7 kV and the SEM-EDS data were collected with a 20 kV electron beam. Bulk SEM-EDS and elemental maps were obtained from drop-casting the $Cu_3(As,Sb)Se_4$ NCs suspended in toluene onto a silicon wafer and analyzed using AZtec software with a standardless quantitative analysis based on the Cliff-Lorimer method. Three random spots were analyzed for each composition to obtain averages and standard deviation for the bulk composition analysis. Size distribution histograms were generated by measuring the horizontal length from the vertical midpoint of over 100 NCs from SEM images using ImageJ software.

Results and Discussion

$Cu_3(As,Sb)Se_4$ Nanocrystals

Prevention of unwanted impurities in NC materials is typically accomplished by adjusting the reactivity of the precursors. In this instance, utilizing stoichiometrically deficient copper precursor was enough to suppress formation of copper sulfide in the NCs. Also, to maintain phase purity of all the $Cu_3(As,Sb)Se_4$ NCs compositions explored, both lower injection and reaction temperatures were required for the Cu_3AsSe_4 NCs compared to the $Cu_3(As,Sb)Se_4$ NCs. The formation of an unknown high temperature copper-arsenic-selenide phase was observed in the Raman spectrum at a synthesis temperature of 250 ˚C (Figure S2). Interestingly, this unknown phase is suppressed with a mixture of arsenic and antimony precursors and requires a higher reaction temperature to form the desired tetragonal $Cu_3(As,Sb)Se_4$ phase described herein.

The synthesized $Cu_3(As,Sb)Se_4$ NCs were imaged using SEM. All NC compositions have relatively similar morphologies, consisting of nanoplates and smaller spherical particles (Figure 1 a-e). The size distribution of the NCs range from as small as approximately 40 nm to more than 400 nm with the majority of the NCs close to 100 nm (Figure 1 f-j). The large size distribution is attributed to the various shapes and aspect ratios of the NCs. To improve the thermoelectric properties, the NC thin films were sintered in a selenium vapor atmosphere at 340 °C for 30 min at 100 Torr. Top-view SEM images of the sintered NCs are seen necking together and sintering in these conditions, forming more densely-packed and larger grains (Figure 1 k-o).

The crystalline phase of the NC alloys was determined using GIXRD (Figure 2). The synthesized Cu_3AsSe_4 and Cu_3SbSe_4 NCs closely match ICSD reference files (collection codes 610361 and 628993, respectively) for a tetragonal crystal structure with an $I\bar{4}2m$ space group. The three main peaks are attributed to the (112) plane near 28°, the (220)/(204) planes near 46° and the (312)/(116) planes near 55°. As the concentration becomes richer in antimony, the (220)/(204) and (312)/(116) planes combine, possibly from a more symmetric crystal structure. The mixed arsenic and antimony alloys show a linear shift in peak locations towards lower diffraction angles with increasing antimony concentration, as predicted by Vegard's law.[29,30]

Assignment of the modes observed in the Raman spectra were based from the previous report by Škácha and co-workers (Figure 3).[31] Discrepancies in the peak positions and intensities are likely due to impurity elements (iron and sulfur) in the reference spectrum as the data were collected from the mineral. For $Cu_3(As,Sb)Se_4$ NCs, Raman modes are shifted to lower frequencies as antimony composition increases. Several groups have reported similar peak shifting phenomenon for other solid solution systems.[32–35] The modes near 230 cm^{-1} appear to be unique to compositions containing antimony; whereas, the modes near 260 cm^{-1} seem to be from arsenic incorporation as both these modes disappear in the absence of antimony or arsenic, respectively. No impurity phases are observed.

The bulk elemental composition of the synthesized NC alloys is close to the target composition as determined by SEM-EDS (Table 1). Often, elemental analysis of bulk NCs results in a non-stoichiometric composition, likely from defect formation, which is commonly reported in the literature.[36–38] A representative SEM-EDS elemental map of the $Cu_3(As_{0.5},Sb_{0.5})Se_4$ alloy NCs shows uniform elemental distribution throughout all the NCs imaged, suggesting impurity free NCs (Figure 4). Elemental maps of all compositions can be found in the Supporting Information (Figure S3).

The ease of synthesis, multiple degrees of property tunability and phase purity of these semiconducting NCs enables exploration into many facets of research. We provide an example of enhanced thermoelectric performance by tuning the relative amounts of arsenic and antimony in the NCs.

Table 1. Bulk scanning electron microscopy energy dispersive X-ray spectroscopy of the synthesized nanocrystal alloys after washing.

	Atomic Fraction		
Desired Composition	$\frac{Cu}{(As+Sb)}$	$\frac{Se}{(Cu+As+Sb)}$	$\frac{As}{Sb}$
Cu_3SbSe_4	2.78 ± 0.04	1.14 ± 0.01	0
$Cu_3(As_{0.25},Sb_{0.75})Se4$	2.81 ± 0.02	1.13 ± 0.00	0.27 ± 0.08
$Cu_3(As_{0.50},Sb_{0.50})Se_4$	2.52 ± 0.20	1.15 ± 0.02	0.51 ± 0.03
$Cu_3(As_{0.75},Sb_{0.25})Se_4$	3.16 ± 0.10	1.08 ± 0.01	0.72 ± 0.07
Cu_3AsSe_4	2.98 ± 0.08	1.06 ± 0.01	1

Thermoelectric Properties. The NC thin films demonstrated very poor thermoelectric performance before heat treating in selenium vapor, likely due to low electrical conductivity resulting from the significant number of grain boundaries in the thin films (Figure 5a). As can be seen in Figure 5b, heat treatment of the NC thin films in a selenium atmosphere for 30 min at 340 °C and 100 Torr pressure resulted in significant necking and sintering of the NCs, greatly improving the electrical conductivity of the thin films. In fact, the thin film composition with the highest thermoelectric performance exhibited a four order of magnitude increase from ~3 ×10-4 S cm^{-1} to ~6 S cm^{-1} in electrical conductivity after only 15 min of heat treatment (Figure S1). The electrical conductivity of all compositions were between 4-6 S cm^{-1}. Furthermore, no significant changes were observed post selenium heat treatment in the GIXRD patterns or Raman spectra (Figures S6-S7). However, the elemental composition seems to become closer to the ideal stoichiometry for $Cu_3(As,Sb)Se_4$ upon heat treatment in selenium (See Table S1).

Electrical conductivity and thermopower measurements for the $Cu_3(As,Sb)Se_4$ thin films indicated p-type behavior (Figure 6) with measured thermopower values on the order of 100-400 μV K^{-1} (Figure 6b) for the thin films operating near room temperature (T = 40˚C).

A champion material power factor of ~112 μW mK^{-2} was obtained for the NC thin films containing equal molar ratios of As and Sb. This power factor value is on the same order of magnitude as the commonly used low-temperature nanoparticle thermoelectric material Bi_2Te_3.[39] The variation in thermoelectric performance as a function of composition is primarily attributed to thermopower enhancement. The observed increase in power factor from the compositions containing both As and Sb is likely the result of a change in the density of states in the electronic structure of the alloy. Similar effects have been reported in the literature for other systems.[40,41] These data demonstrate the ability to use the controlled synthetic scheme presented above to precisely tune the material properties of the resultant NC thin film. We expect this same paradigm can be readily extended to other energy conversion applications based upon the robustness of the synthetic protocol.

Conclusions

We report the synthesis and characterization of a series of earth abundant $Cu_3(As,Sb)Se_4$ alloy NCs thin films possessing relatively high room temperature thermoelectric properties. Raman and XRD analysis verified the $Cu_3(As,Sb)Se_4$ NCs to be impurity-free with a tetragonal crystal structure. SEM-EDS and elemental mapping highlighted the compositions of the NCs were close to the target compositions with uniformly distributed elements throughout the NCs. The average size and morphology of the NCs was close to 100 nm for all compositions and consisted of various shapes (*e.g.*, nanoplates and nanobricks). By heat treating the NC thin films in a selenium atmosphere, the NCs sintered into a dense thin film network resulting in significantly enhanced thermoelectric performance. A champion power factor of 112 μW m^{-1} K^{-2} was achieved for the composition containing equal molar ratios of As and Sb. While a power factor of this magnitude is lower than some currently available thermoelectric materials, the solution-processability, earth abundance of the constituent elements comprising the $Cu_3(As,Sb)Se_4$ alloy NCs and novel heat treatment in a selenium atmosphere opens many new doors to tuning these readily-scalable NC alloys. As such, the work presented herein provides a clear pathway for the development of $Cu_3(As,Sb)Se_4$ NC based, next-generation room temperature thermoelectric materials.

Acknowledgements

R.A. and R.B.B. acknowledge financial support via the NSF Solar Economy IGERT (0903670-DGE) program. The work of E.P.T. and B.W.B. was made possible through a Defense Advanced Research Projects Agency (DARPA) Young Faculty Award (DARPA YFA, Grant Number: N66001-12-1-4253), and they gratefully acknowledge this support.

References

1 Lawrence Livermore National Laboratory and the Department of Energy, 2014.
2 F. J. DiSalvo, *Science*, 1999, **285**, 703–706.
3 H. J. Goldsmid, *Thermoelectric Refrigeration*, Plenum Press, New York, 1964.
4 G. J. Snyder and E. S. Toberer, *Nat. Mater.*, 2008, **7**, 105–114.
5 A. Shakouri, *Annu. Rev. Mater. Res.*, 2011, **41**, 399–431.
6 R. Venkatasubramanian, E. Siivola, T. Colpitts and B. O'Quinn, *Nature*, 2001, **413**, 597–602.
7 Y. Pei, A. D. LaLonde, N. a. Heinz and G. J. Snyder, *Adv. Energy Mater.*, 2012, **2**, 670–675.
8 T. C. Harman, P. J. Taylor, M. P. Walsh and B. E. LaForge, *Science*, 2002, **297**, 2229–2232.
9 G. Chen, *Phys. Rev. B*, 1998, **57**, 14958–14973.
10 M. S. Dresselhaus, G. Chen, M. Y. Tang, R. Yang, H. Lee, D. Wang, Z. Ren, J. P. Fleurial and P. Gogna, *Adv. Mater.*, 2007, **19**, 1043–1053.
11 M. G. Kanatzidis, *Chem. Mater.*, 2010, **22**, 648–659.
12 Y. Lan, A. J. Minnich, G. Chen and Z. Ren, *Adv. Funct. Mater.*, 2010, **20**, 357–376.
13 S. I. Kim, K. H. Lee, H. A. Mun, H. S. Kim, S. W. Hwang, J. W. Roh, D. J. Yang, W. H. Shin, X. S. Li, Y. H. Lee, G. J. Snyder and S. W. Kim, *Science*, 2015, **348**, 109–114.
14 N. Mingo, D. Hauser, N. P. Kobayashi, M. Plissonnier and A. Shakouri, *Nano Lett.*, 2009, **9**, 711–715.
15 X. Y. Li, D. Li, H. X. Xin, J. Zhang, C. J. Song and X. Y. Qin, *J. Alloys Compd.*, 2013, **561**, 105–108.
16 T.-R. Wei, H. Wang, Z. M. Gibbs, C.-F. Wu, G. J. Snyder and J.-F. Li, *J. Mater. Chem. A*, 2014, **2**, 13527.
17 B. Poudel, Q. Hao, Y. Ma, Y. Lan, A. Minnich, B. Yu, X. Yan, D. Wang, A. Muto, D. Vashaee, X. Chen, J. Liu, M. S. Dresselhaus, G. Chen and Z. Ren, *Science*, 2008, **320**, 634–638.
18 K. F. Hsu, S. Loo, F. Guo, W. Chen, J. S. Dyck, C. Uher, T. Hogan, E. K. Polychroniadis and M. G. Kanatzidis, *Science*, 2004, **303**, 818–821.
19 D. Chung, T. Hogan, P. Brazis, M. Rocci-Lane, C. Kannewurf, M. Bastea, C. Uher and M. G. Kanatzidis, *Science*, 2000, **287**, 1024–1027.

20 Y. Gelbstein, Z. Dashevsky and M. P. Dariel, *Phys. B Condens. Matter*, 2005, **363**, 196–205.
21 S. E. Habas, H. A. S. Platt, M. F. A. M. van Hest and D. S. Ginley, *Chem. Rev.*, 2010, **110**, 6571–6594.
22 S. B. Fuller, E. J. Wilhelm and J. M. Jacobson, *J. Microelectromechanical Syst.*, 2002, **11**, 54–60.
23 K. Tyagi, B. Gahtori, S. Bathula, V. Toutam, S. Sharma, N. K. Singh and A. Dhar, *Appl. Phys. Lett.*, 2014, **105**, 261902.
24 D. Li, R. Li, X.-Y. Qin, C.-J. Song, H.-X. Xin, L. Wang, J. Zhang, G. Guo, T.-H. Zou, Y.-F. Liu and X.-G. Zhu, *Dalton Trans.*, 2014, **43**, 1888–96.
25 E. J. Skoug, J. D. Cain and D. T. Morelli, in *MRS Proceedings*, 2011, vol. 1314, pp. 13–18.
26 E. J. Skoug, J. D. Cain and D. T. Morelli, *Appl. Phys. Lett.*, 2011, **98**, 261911.
27 E. J. Skoug, J. D. Cain, D. T. Morelli, M. Kirkham, P. Majsztrik and E. Lara-Curzio, *J. Appl. Phys.*, 2011, **110**, 023501.
28 B. C. Walker and R. Agrawal, *Chem. Commun.*, 2014, **50**, 8331–4.
29 L. Vegard, *Zeitschrift für Phys.*, 1921, **5**, 17–26.
30 A. R. Denton and N. W. Ashcroft, *Phys. Rev. A*, 1991, **43**, 3161–3164.
31 P. Škácha, E. Buixaderas, J. Plášil, J. Sejkora, V. Goliáš and V. Vlček, *Can. Mineral.*, 2014, **52**, 501–511.
32 I. F. Chang and S. S. Mitra, *Adv. Phys.*, 1971, **20**, 359–404.
33 N. Kornienko, D. D. Whitmore, Y. Yu, S. R. Leone and P. Yang, *ACS Nano*, 2015, **9**, 3951–3960.
34 M. Park, S. Ahn, J. H. Yun, J. Gwak, A. Cho, S. Ahn, K. Shin, D. Nam, H. Cheong and K. Yoon, *J. Alloys Compd.*, 2012, **513**, 68–74.
35 T. Prokofyeva, T. Sauncy, M. Seon, M. Holtz, Y. Qiu, S. Nikishin and H. Temkin, *Appl. Phys. Lett.*, 1998, **73**, 1409–1411.
36 R. B. Balow, E. J. Sheets, M. M. Abu-Omar and R. Agrawal, *Chem. Mater.*, 2015, **27**, 2290–2293.
37 Y.-K. Kim, S.-H. Ahn, K. Chung, Y.-S. Cho and C.-J. Choi, *J. Mater. Chem.*, 2012, **22**, 1516.
38 S. Chen, A. Walsh, X. G. Gong and S. H. Wei, *Adv. Mater.*, 2013, **25**, 1522–1539.
39 Y. Zhao, J. S. Dyck, B. M. Hernandez and C. Burda, *J. Phys. Chem. C*, 2010, **114**, 11607–11613.
40 D. Bilc, S. D. Mahanti, E. Quarez, K. F. Hsu, R. Pcionek and M. G. Kanatzidis, *Phys. Rev. Lett.*, 2004, **93**, 12–15.
41 C. M. Jaworski, B. Wiendlocha, V. Jovovic and J. P. Heremans, *Energy Environ. Sci.*, 2011, **4**, 4155.

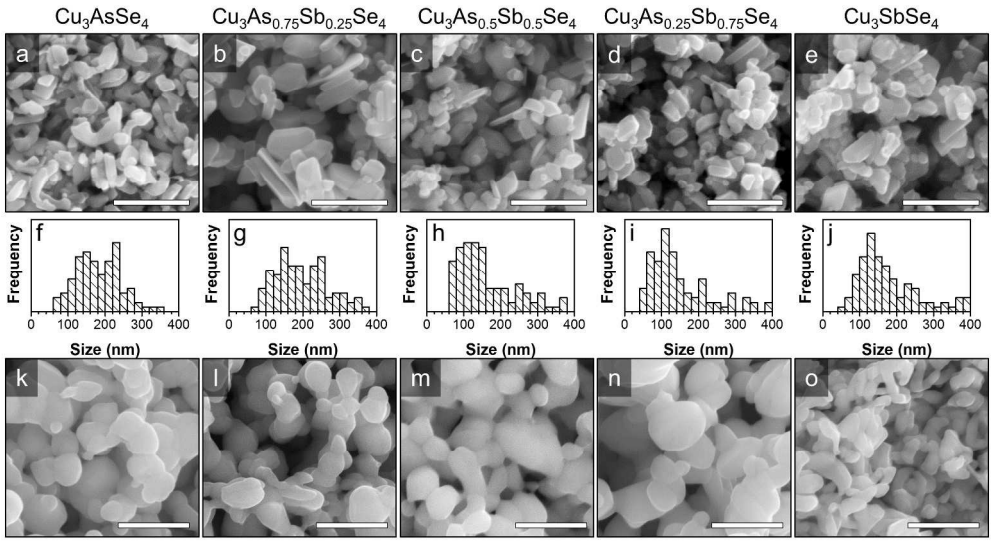

Figure 1. Top-view scanning electron microscopy (SEM) images of the drop-casted thin films of $Cu_3(As,Sb)Se_4$ nanocrystals (a-e). The nanocrystals have a diverse morphology ranging from nanoplates with various aspect ratios to smaller, more spherical particles. The size distribution of the nanocrystals (f-j) varies from as small as 40 nm to over 400 nm with an average size of ~100 nm. The different shapes and aspect ratios of the nanocrystals play significant roles in the broadening of the size distribution. (k-o) Top-view SEM images of the thin films after heat treatment in a selenium vapor atmosphere showing the nanocrystals necking together and sintering, creating denser, yet still porous, thin films. The scale bars are all representative of 1 μm.
264x143mm (300 x 300 DPI)

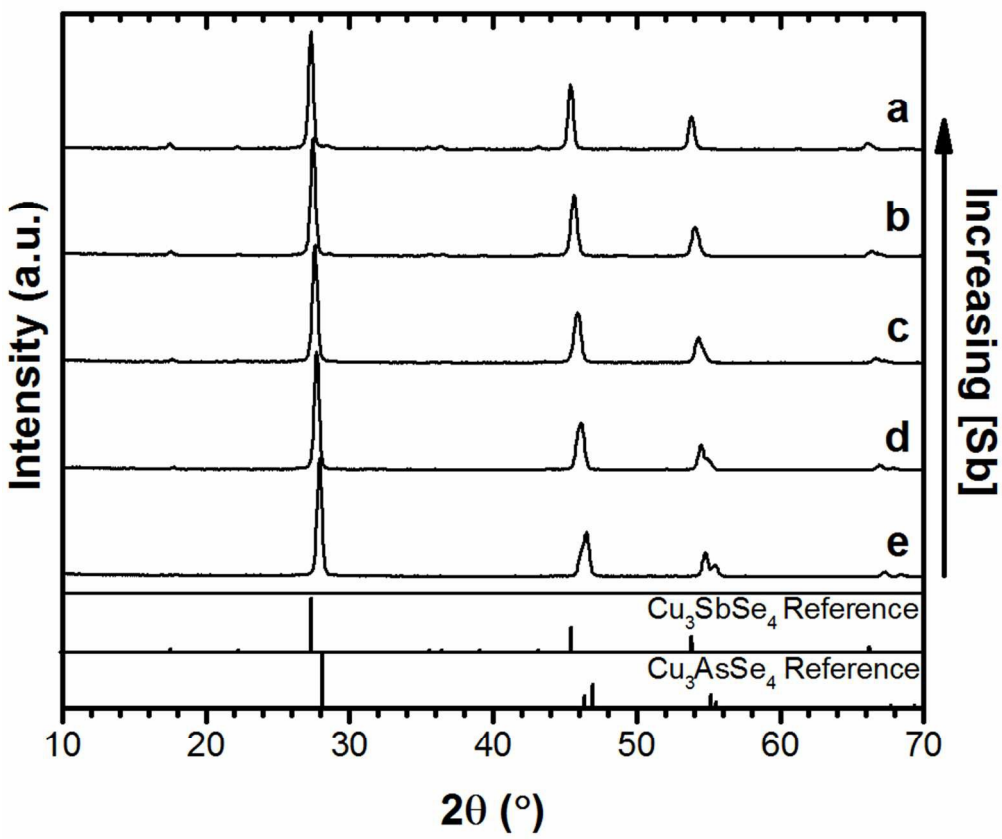

Figure 2. Grazing incidence X-ray diffraction patterns of phase pure (a) Cu_3SbSe_4, (b) $Cu_3(As_{0.25},Sb_{0.75})Se_4$, (c) $Cu_3(As_{0.50},Sb_{0.50})Se_4$, (d) $Cu_3(As_{0.75},Sb_{0.25})Se_4$ and (e) Cu_3AsSe_4 nanocrystal thin films showing a linear shift in peak position with increasing antimony concentration. No impurity phases are detected. For reference, Cu_3SbSe_4 (ICSD Collection Code 628993) and Cu_3AsSe_4 (ICSD Collection Code 610361) are provided.
82x69mm (300 x 300 DPI)

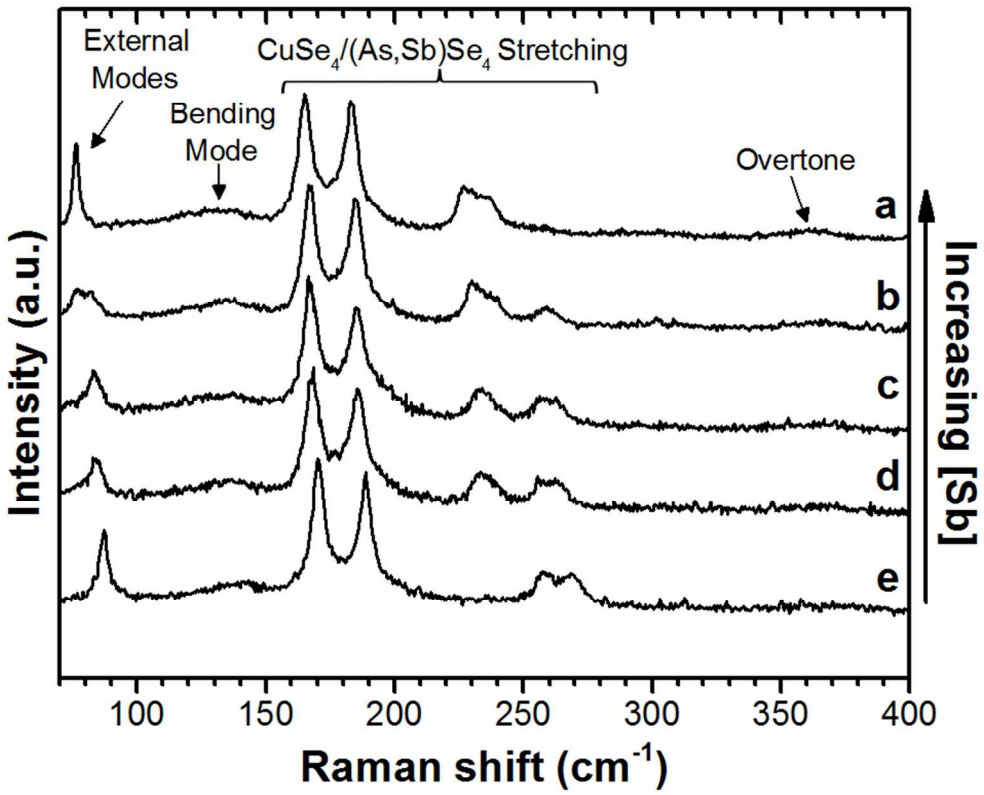

Figure 3. Raman spectra of (a) Cu_3SbSe_4, (b) $Cu_3(As_{0.25},Sb_{0.75})Se_4$, (c) $Cu_3(As_{0.50},Sb_{0.50})Se_4$, (d) $Cu_3(As_{0.75},Sb_{0.25})Se_4$ and (e) Cu_3AsSe_4 nanocrystal thin films showing similar features for all compositions. A shift to lower wavenumbers is observed with increasing concentration of antimony in the NCs. No impurity phases are detected.
82x65mm (300 x 300 DPI)

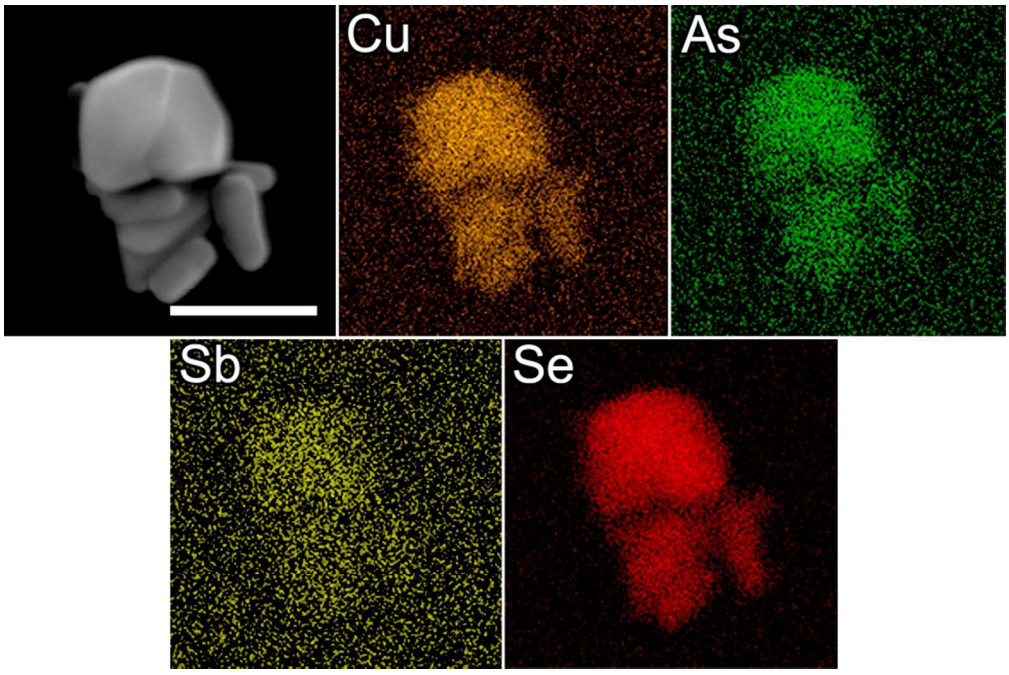

Figure 4. Scanning electron microscopy energy dispersive X-ray spectroscopy elemental maps depicting uniform elemental distribution throughout the $Cu_3(As_{0.50},Sb_{0.50})Se_4$ nanocrystals. The scale bar represents 500 nm.
82x54mm (300 x 300 DPI)

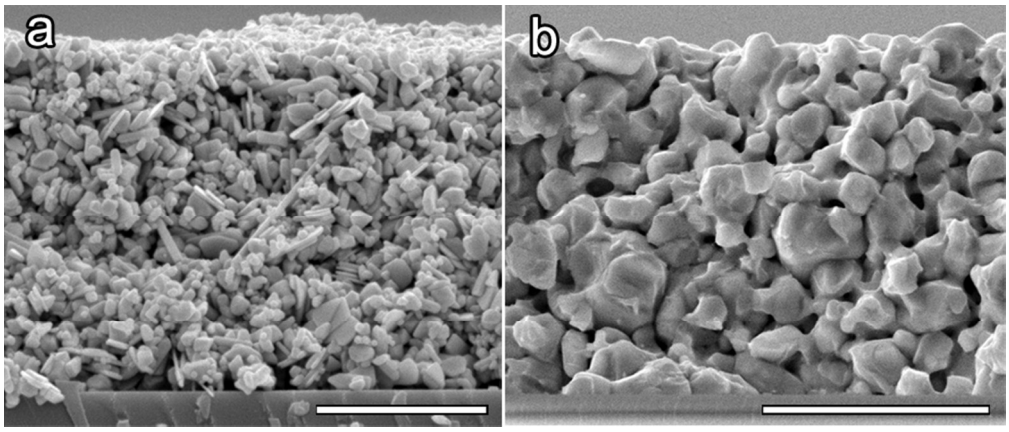

Figure 5. Cross sectional scanning electron microscopy images of $Cu_3(As_{0.50},Sb_{0.50})Se_4$ thin films (a) before and (b) after heat treatment in a selenium atmosphere. The grain size dramatically increases after selenium heat treatment resulting in significant improvement in thermoelectric performance. The scale bars represent 3 μm.
82x34mm (300 x 300 DPI)

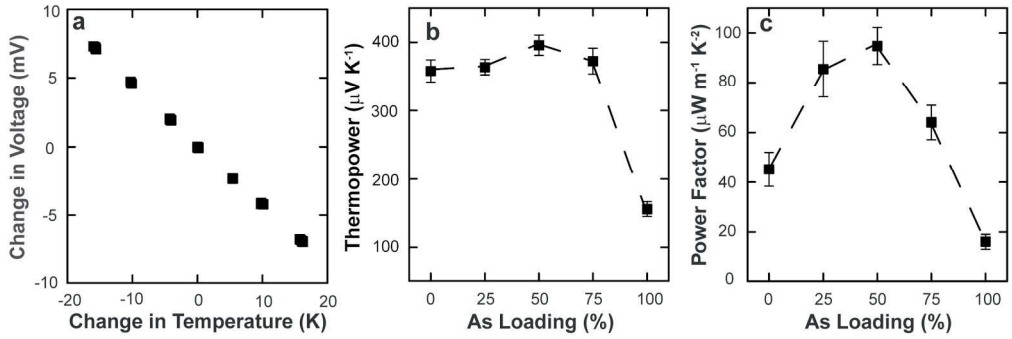

Figure 6. (a) Thermopower measurement at an average temperature of 313 K showing p-type behavior (negative slope) with a performance of 426 μV K^{-1}. (b) Thermopower as a function of nanocrystal composition. Multiple thin films were averaged for each data point and the data point represents the average value. The error bars represent the standard error in the thin films relative to the average. (c) The thermoelectric power factor is represented as a function of nanocrystal composition. Note the highest performing thin films exist for a nanocrystal composition of equal molar ratios of As and Sb.
178x59mm (300 x 300 DPI)

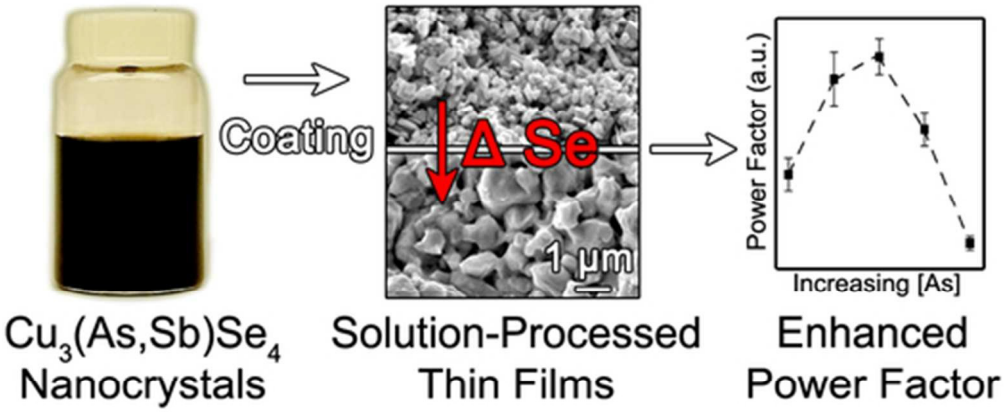

Graphical Abstract
44x23mm (300 x 300 DPI)